City, University of London Institutional Repository

This is the accepted version of the paper.

This version of the publication may differ from the final published version.

Heating effects during bubble collapse using tabulated data

[1]Nikolaos Kyriazis*; [1]Phoevos Koukouvinis; [1]Manolis Gavaises; [2]Richard Pearson and [2]Martin Gold

[1]City, University of London, London, UK

[2]BP International Ltd, UK

Abstract

An explicit density-based solver for the compressible Navier-Stokes equations able to simulate cavitating flows has been developed and utilised for the simulation of collapsing vapour bubbles. Phase-change is considered by employing the homogeneous equilibrium model (HEM). The wide variation of Mach numbers between the liquid, vapour and mixture regimes is tackled by a Mach consistent numerical flux, suitable for subsonic up to supersonic flow conditions. Time discretisation is performed using a second order low storage Runge-Kutta scheme. Thermodynamic closure is achieved by utilising the Helmholtz energy equation of state (EoS), making feasible simulation of conditions at subcritical and supercritical regions considering the variations of liquid and vapour temperatures during bubble collapse. In order to reduce the computational cost associated with the solution of the Helmholtz EoS at each time step, a tabulated data technique has been followed. The unstructured thermodynamic table, containing the thermodynamic properties derived from the Helmholtz EoS, has been constructed for n-dodecane, which has been the considered as the working fluid. The efficiency of the method is enhanced by a static linked-list algorithm for searching among the elements of the table. In addition, a finite element bilinear interpolation is used for approximating the unknown thermodynamic properties. After validating the numerical method, parametric studies considering 2-D axisymmetric vaporous bubble collapse in the proximity of a wall have been performed at conditions realised in micro-orifice flow passages. The temperature and pressure changes on the wall are estimated as function of the surrounding liquid pressure, the initial bubble radius and the location of the wall from the center of the initial bubble, revealing the expected range of variation as function on the set parameters.

Keywords: bubble dynamics; cavitation; Helmholtz equation of state; exact Riemann solver

Introduction

Several numerical studies have been performed regarding vapour bubble dynamics, since they have numerous industrial and physical applications. Different methodologies such as potential flow solvers [1], homogeneous equilibrium mixture (HEM) models [2], interface capturing and interface tracking methods have been employed. In HEM models the phase change is predicted by the density variation and the main assumption is that the two phases are in mechanical and thermodynamic equilibrium. HEM methods have become popular due to their simplicity and because no empirical parameters are needed. On the other hand, interface tracking methods, such as front tracking methods [3], offer sharp interface and they also allow large deformations of the surface. Similar are the interface capturing methods, such as Volume of Fluid (VOF) approach [4] and Level Set Method [5]. Although the main feature of interface capturing methods is again sharp interface, in conditions close to the critical point there is not a clear distinction between the two phases. In the majority of the previous works thermal effects have been ignored, for example in barotropic models, or temperature effects have been taken into account by the use of simplified EoS, such as stiffened gas EoS or similar. The current study expands the previous work of Koukouvinis et al. [6] by examining the heating effects during the collapse of a vapour bubble. The thermodynamic closure in the HEM is achieved by the Helmholtz energy EoS from NIST Refprop databases [7], both for subcritical and for supercritical conditions. A tabulated form of the Helmholtz energy EoS has been implemented in the solver for higher numerical efficiency.

Numerical Method

The numerical method has been described in detail and validated in [8], here only the main features are discussed. The 2-D Euler equations in r-z cylindrical coordinates with a geometric source term accounting for cylindrical symmetry are explicitly solved [9]:

*Corresponding Author, Nikolaos Kyriazis: Nikolaos.Kyriazis@city.ac.uk

$$\mathbf{U}_t + \mathbf{F}(\mathbf{U})_r + \mathbf{G}(\mathbf{U})_z = \mathbf{S}(\mathbf{U}), \ in \ \Omega \tag{1}$$

Where t, r, z subscripts denote differentiation with respect to time, r direction and z direction respectively. $\mathbf{U}$ is the conserved variable vector, $\mathbf{F}(\mathbf{U})$ and $\mathbf{G}(\mathbf{U})$ are the fluxes at the radial (r) and axial (z) directions respectively and $\mathbf{S}(\mathbf{U})$ is the geometric source term:

$$\mathbf{U} = \begin{bmatrix} \rho \\ \rho u_r \\ \rho u_z \\ \rho E \end{bmatrix}, \ \mathbf{F}(\mathbf{U}) = \begin{bmatrix} \rho u_r \\ \rho u_r^2 + p \\ \rho u_r u_z \\ (\rho E + p)u_r \end{bmatrix}, \ \mathbf{G}(\mathbf{U}) = \begin{bmatrix} \rho u_z \\ \rho u_r u_z \\ \rho u_z^2 + p \\ (\rho E + p)u_z \end{bmatrix}, \ \mathbf{S}(\mathbf{U}) = -\frac{s}{r}\begin{bmatrix} \rho u_r \\ \rho u_r^2 \\ \rho u_r u_z \\ u_r(\rho E + p) \end{bmatrix} \tag{2}$$

where ρ is the fluid density, u_r and u_z the radial and axial velocity components respectively, p is the pressure, E is the total internal energy, equal to $\frac{1}{2}\left(u_r^2 + u_z^2\right) + e$, e is the internal energy of the fluid and s is the geometric source term. For cylindrical symmetry, s is equal to unity. The viscosity and the surface tension are neglected in the present study since the phenomenon is inertia driven [10].

The properties of n-Dodecane are derived from the Helmholtz energy. The Helmholtz energy is calibrated within the temperature range 263.6 K$\leq$T$\leq$700 K, for maximum pressure p_{max}=700 MPa and for maximum density ρ_{max}=771.62 kg/m^3 [7]. The dimensionless form of the aforementioned EoS, having as independent variables the density and the temperature is given by:

$$\frac{a(\rho,T)}{RT} = \alpha(\delta,\tau) = \alpha^0(\delta,\tau) + \alpha^r(\delta,\tau) \tag{3}$$

Where $\delta = \rho/\rho_c$, $\tau = T_c/T$. From equation (3) all the thermodynamic properties can be obtained, such as pressure, internal energy, enthalpy and speed of sound as a function of density and temperature. The saturation conditions are identified by the Maxwell criterion and the fluid properties in the saturation dome are calculated by the mixture assumption, whereas the mixture speed of sound is determined from the Wallis speed of sound formula [11].

Instead of solving the Helmholtz EoS for each time step, a tabulated technique, similar to Dumbser et al. [12] has been implemented after explicitly solving the Euler equations. An unstructured thermodynamic table of approximately 40,000 elements, refined around the saturation curve, which contains all the thermodynamic properties has been created. Then the thermodynamic table has been split into smaller data groups by static linked lists in order to search only in the group with the desired properties within its range. Since the density and the internal energy are calculated by the Euler equations, the corresponding element of the table is identified through numerical inversion from the above quantities. Any thermodynamic property φ (pressure, temperature or speed of sound) within a specific element of the table is then approximated by a Finite Element bilinear interpolation:

$$\varphi(\rho,e) = \sum_{n}^{nodes} N_n(\rho,e)b_n \tag{4}$$

Where b are the unknown coefficients of φ and N is the shape function of node n:

$$N_n(\rho,e) = 1 + (e - e_n) + (\rho - \rho_n) + (e - e_n)(\rho - \rho_n) \tag{5}$$

And the coefficients of each property are calculated by:

$$\mathbf{b} = [\mathrm{N}]^{-1}\boldsymbol{\varphi} \tag{6}$$

Where $\boldsymbol{\varphi}$ are the values of the property at the nodes of the quadrilateral element and N is given by:

$$N_{mn} = 1 + (e_m - e_n) + (\rho_m - \rho_n) + (e_m - e_n)(\rho_m - \rho_n) \tag{7}$$

A Mach number consistent numerical flux has been implemented [13] in order to handle the great variation of the Mach number between the liquid and the vapour regimes. Time discretisation has been achieved by a low storage four-stage Runge-Kutta method, 2nd order in time.

Results

*Corresponding Author, Nikolaos Kyriazis: Nikolaos.Kyriazis@city.ac.uk

In this section the results of a parametric bubble collapse are presented. The collapse of a vapour bubble in the vicinity of a wall is investigated for a different set of configurations (see Table 1 and [8] for details concerning the configuration). In Table 1 the ratio $d_w/R_{b,0}$ is the distance from the wall to the center of the bubble divided by the initial bubble radius, p_{inf} is the pressure of the liquid, T is the initial temperature for both the liquid and the vapour and τ is the Rayleigh collapse time for each case. The density of the vapour bubble for all the cases is $\rho_{vap}=33.78 \ kg/m^3$. The computational domain is *20* times the initial bubble radius and *200* equally spaced cells have been used along the initial radius. This ratio has been kept for distance of $2.5R_{b,0}$ from the origin and then the mesh is coarsened with ratio *1.05* in both directions. Zero gradient boundary condition has been used for the right and the upper side, slip wall for the lower side, whereas for the y-axis of symmetry, the normal velocity component is zero.

No	$d_{w,0}/R_{b,0}$	$R_{b,0}$ (*μm*)	p_{inf} (*bar*)	*T* (*K*)	τ (*s*)
1	1.5	1	10	400	2.37e-08
2	1.5	10	10	400	2.37e-07
3	1.5	1	100	400	7.55e-09
4	1.5	10	100	400	7.55e-08
5	0	1	10	400	2.37e-08
6	0	10	10	400	2.37e-07
7	0	1	100	400	7.55e-09
8	0	10	100	400	7.55e-08
9	-0.5	1	10	400	2.37e-08
10	-0.5	10	10	400	2.37e-07
11	-0.5	1	100	400	7.55e-09
12	-0.5	10	100	400	7.55e-08

Table 1. *Classification of the different cases examined.*

In Figure 1 the volume of vapour (left), the maximum pressure on the wall (middle) and the maximum temperature on the wall (right) are shown with respect to time. Regarding Figure 1a, the collapse time is proportional to the initial volume of the vapour for each bubble. A rebound is noticed for cases 1-4, however it is weaker than the one noticed in [8], due to the larger distance between the wall and the center of the bubble. The early pressure peaks at *Time<0.5* for cases 1, 2 and at *Time<0.8* for cases 3, 4 (Figure 1b) are because of the collapse of a vapour region below the bubble which was originally created by a rarefaction wave (see also [8]). A pressure and temperature peak (total maximum) due to the bubble collapse is noticed in Figure 1b and Figure 1c at *Time~1* for cases 1-8 and at *Time~0.7* for cases 9-12. However, at cases 1-4 are noticed the lowest wall pressures and the lowest wall temperatures because most of the energy is transformed into kinetic and as a consequence the pressure increase is not as significant as in the rest cases; the same applies for the temperature. On the contrary, at cases 5-8 the maximum wall pressures and the maximum wall temperatures are noticed due to the maximum compression that the bubble undergoes during its collapse. After the collapse of the bubble (*Time>1.5*), additional pressure peaks are noticed for cases 1-4, because of the collapse of the regenerated vapour regions. The pressure increase due to the re-entrant jet and the shock wave after the collapse can potentially lead to erosion damage of materials. For all three figures the curves between cases with different initial radius but the same surrounding pressure and the same distance d_w coincide, as it was expected, given the fact that the time has been non-dimensionalised with τ.

(a)   (b)   (c)

*Corresponding Author, Nikolaos Kyriazis: Nikolaos.Kyriazis@city.ac.uk
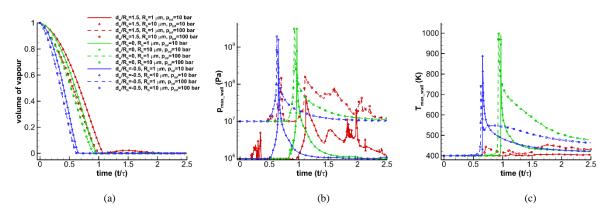
Figure 1. *Volume of vapour (left), maximum wall pressure (middle) and maximum wall temperature (right) with respect to time for different vapor bubble configurations. Time has been non-dimensionalized with the Rayleigh collapse time τ and the volume of vapour with the initial vapour volume of the bubble.*

In Figure 2 the pressure (left slice) and the temperature (right slice) contour fields are demonstrated for several time instances during the collapse for case No 1. At *Time=0.1* the shape of the bubble is almost spherical in comparison with [6], [8] where a heart-shape was formed. This is due to the larger distance of the bubble from the wall, therefore the effect of the boundary is weaker than the aforementioned studies. The bubble takes a non-spherical heart-like shape only at later times just before the collapse, when the micro-jet has already been formed on the top of the bubble and the pressure field has been developed (*Time=1.05* and *Time=1.07*). By that time there is no significant temperature variation. However, at the moment of the collapse (*Time=1.08*), there is a significant pressure increase up to *1600 MPa* and a temperature increase up to *550 K* due to the condensation of the bubble. Finally, at *Time=1.1* the shock wave travelling away from the axis of symmetry is shown.
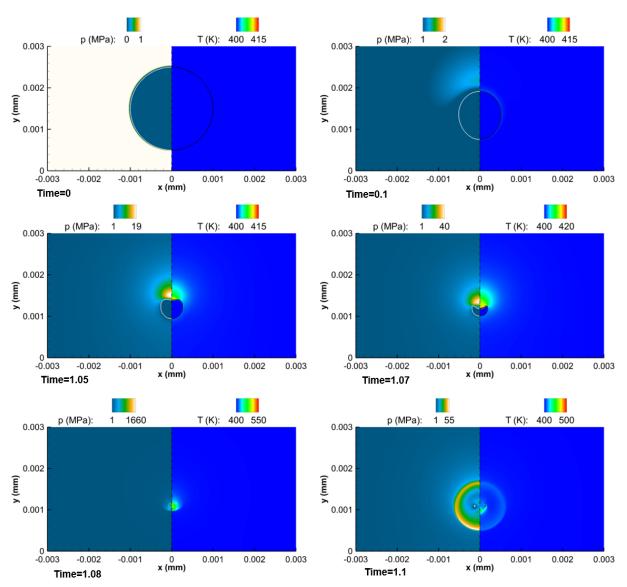

Figure 2. *Instances during the vapour bubble collapse for case No 1. Time has been non-dimensionalized with Rayleigh collapse time. Pressure field (left slice) and temperature field (right slice) are shown.*

Conclusions

*Corresponding Author, Nikolaos Kyriazis: Nikolaos.Kyriazis@city.ac.uk

In the present work, a HEM approach combined with real fuel thermodynamics has been presented and utilized for vaporous bubble collapse simulations. A parametric study of the temperature and pressure changes on the wall with respect to the surrounding liquid pressure, the initial bubble radius and the distance of the wall from the center of the initial bubble has been performed. It can be concluded that the temperature increase during bubble collapse is not negligible, for example in cases 5-8 it can reach up to *1000 K*. The maximum pressure and temperature increase is observed when the center of the initial bubble is on the wall (spherical symmetry). These heating effects during bubble collapse can possibly have implications in injector nozzles, since they can change the fuel properties and have a serious impact on the flow field.

References

[1] Q. Wang, "Multi-oscillations of a bubble in a compressible liquid near a rigid boundary," *Journal of Fluid Mechanics*, vol. 745, pp. 509–536, 004 2014.

[2] N. A. Adams and S. J. Schmidt, "Shocks in Cavitating Flows," in *Bubble Dynamics and Shock Waves*, F. C. Delale, Ed. Berlin, Heidelberg: Springer Berlin Heidelberg, 2013, pp. 235–256.

[3] S. T. Popinet, Eacute, Phane, S. T. Zaleski, Eacute, and Phane, "Bubble collapse near a solid boundary: a numerical study of the influence of viscosity," *Journal of Fluid Mechanics*, vol. 464, pp. 137–163, 2002.

[4] B. B. Li, W. Jia, H. C. Zhang, and J. Lu, "Investigation on the collapse behavior of a cavitation bubble near a conical rigid boundary," *Shock Waves*, vol. 24, pp. 317–324, 2014.

[5] E. Lauer, X. Y. Hu, S. Hickel, and N. A. Adams, "Numerical modelling and investigation of symmetric and asymmetric cavitation bubble dynamics," *Computers & Fluids*, vol. 69, pp. 1–19, 30 2012.

[6] P. Koukouvinis, M. Gavaises, A. Georgoulas, and M. Marengo, "Compressible simulations of bubble dynamics with central-upwind schemes," *International Journal of Computational Fluid Dynamics*, pp. 1–12, 2016.

[7] E. W. Lemmon and M. L. Huber, "Thermodynamic Properties of n-Dodecane," *Energy & Fuels*, vol. 18, pp. 960–967, Jul. 2004.

[8] N. Kyriazis, P. Koukouvinis, and M. Gavaises, "Numerical investigation of bubble dynamics using tabulated data," *International Journal of Multiphase Flow*, vol. 93, no. Supplement C, pp. 158–177, Jul. 2017.

[9] E. F. Toro, *Riemann Solvers and Numerical Methods for Fluid Dynamics, A Practical Introduction*. Springer Berlin Heidelberg, 2009.

[10] S. Zhang, J. H. Duncan, and G. L. Chahine, "The final stage of the collapse of a cavitation bubble near a rigid wall," *Journal of Fluid Mechanics*, vol. 257, pp. 147–181, 1993.

[11] Brennen C. E., *Cavitation and Bubble Dynamics*. 1995.

[12] M. Dumbser, U. Iben, and C.-D. Munz, "Efficient implementation of high order unstructured WENO schemes for cavitating flows," *Computers & Fluids*, vol. 86, pp. 141–168, 5 2013.

[13] S. Schmidt, I. Sezal, G. Schnerr, and M. Talhamer, "Riemann Techniques for the Simulation of Compressible Liquid Flows with Phase-Transistion at all Mach Numbers - Shock and Wave Dynamics in Cavitating 3-D Micro and Macro Systems," in *46th AIAA Aerospace Sciences Meeting and Exhibit*, 0 vols., American Institute of Aeronautics and Astronautics, 2008.

*Corresponding Author, Nikolaos Kyriazis: Nikolaos.Kyriazis@city.ac.uk